

# Gamma-ray variability and multi-wavelength insights into the unprecedented outburst from 4C 31.03

Aminabi Thekkoth<sup>a,\*</sup>, Baheeja C<sup>a</sup>, S Sahayanathan<sup>b,c</sup> and C D Ravikumar<sup>a</sup>

<sup>a</sup>University of Calicut, Thenjippalam, Malappuram, 673635, Kerala, India

<sup>b</sup>Bhabha Atomic Research Centre, Mumbai, 400085, Maharashtra, India

<sup>c</sup>Homi Bhabha National Institute, Mumbai, 400094, Maharashtra, India

## ARTICLE INFO

### Keywords:

galaxies:active

quasars:individual(4C 31.03)

radiation mechanisms:non-thermal

method:data analysis

gamma rays

## ABSTRACT

The blazar 4C 31.03 recently underwent a major  $\gamma$ -ray outburst at the beginning of 2023 after a prolonged quiescent phase. *Fermi*-LAT reported a daily average flux of  $5 \times 10^{-6}$  phs  $\text{cm}^{-2} \text{s}^{-1}$ , which is about 60 times its average value. We investigated this extraordinary outbreak through temporal and multi-wavelength analysis. From the statistical analysis of the  $\gamma$ -ray lightcurves using Bayesian blocks, we identified 3 epochs of prominent flares. The fastest flux decay during this major outburst was observed within  $5.5 \pm 0.7$  hours. The highest energy of  $\gamma$ -ray photons found from the source during the active phase is  $\sim 82$  GeV. Using the transparency of  $\gamma$ -rays against pair production and light crossing time argument, we could obtain the minimum jet Doppler factor as 17 corresponding to the flaring state. The broadband spectral energy distribution study performed using synchrotron, SSC and EC emission processes supports the external Compton scattering of IR photons as the likely mechanism for the  $\gamma$ -ray emission from the source. The results of this study suggest the scenario of the emission region in 4C 31.03, being located beyond the Broad line region from the central blackhole. Long-term  $\gamma$ -ray flux distribution of 4C 31.03 depicts a double log-normal variability, indicating that two distinct flux states are active in this energy band. The index distribution also reveals a two distinct variability patterns, suggesting that the  $\gamma$ -ray spectrum can be more precisely described by two photon indices.

## 1. Introduction

*Fermi*-LAT is a  $\gamma$ -ray space telescope, that observes the cosmos in the energy range 20 MeV to 1 TeV. With a wide field of view, LAT scans the entire sky every 3 hours. Recently, in January 2023, *Fermi*-LAT reported an enhancement in the  $\gamma$ -ray activity from the source 4C 31.03, consistent with the coordinates RA=18.2227 and DEC=32.1399 [1]. 4C 31.03 is recognized as a flat spectrum radio quasar (FSRQ) ( $z=0.603$ , [2]) and is included in the *Fermi* 4FGL point source catalog with identifier J0112.8+3208 [3]. This source is also historically known in other names such as, B2 0110+31, OC 317, and NRAO 62. Further, it is considered as a possible candidate for the study of neutrino emission from Blazars ([4]). This recent high  $\gamma$ -ray outburst marks the first instance of such an extraordinary activity since its discovery. The daily average gamma-ray flux reported ( $\sim 4 \times 10^{-6}$  phs  $\text{cm}^{-2} \text{s}^{-1}$ ) is 60 times greater than the average value quoted in the 4FGL catalog. Following this, the IceCube Collaboration has conducted a search for possible muon neutrino events from the source and obtained an upper limit on the neutrino flux, with a 90% confidence level [5]. After this flaring event, the source reverted back to its quiescent flux level within a few days. The source again underwent a major transition to the phase of high activity during June 2023 with a maximum flux of  $4.9 \times 10^{-6}$

phs  $\text{cm}^{-2} \text{s}^{-1}$  [6]. The variability aspects of this source has not been thoroughly studied before, despite continuous monitoring by *Fermi*-LAT since 2009.

Under the unified model of radio-loud active galactic nuclei, blazars form the subclass with their relativistic jet pointed towards the earth [7]. The relativistic effects boost the intrinsic emission from blazars making them extremely luminous in the universe. Their high luminosity in  $\gamma$ -rays makes them the primary target of *Fermi*-LAT. FSRQs are the luminous category of blazars with maximum power emitted at gamma-ray energies [8, 9, 10]. These objects exhibit strong continuum emission lines in the optical spectrum whereas, BL Lacs have featureless optical spectra [7, 11]. The spectral energy distribution (SED) of blazars is non-thermal spanning from radio to gamma-rays and features two broad peaks. The frequency at which the low-energy SED component peaks varies among the blazar classes, with FSRQ's having the least peak energy falling around infrared frequency [8, 12].

The theoretical models which are used to interpret the observed broadband SED of blazars, fall mainly under two emission scenarios namely leptonic and/or hadronic origin [13]. Under both these scenarios, the lower energy spectral component has been well understood to be synchrotron emission from a relativistic population of non-thermal electrons in the jet [14, 15]. However, the underlying mechanism for the higher-energy (HE) emission and the location of the main emission region from the central blackhole, still remain as open questions [16]. Leptonic models interpret the higher energy SED via inverse Compton scattering of soft photons which can be synchrotron photon itself (SSC)

\*Corresponding author

✉ thekkothaminabi@gmail.com (A. Thekkoth); baheeja314@gmail.com (B. C.); sunder@barc.gov.in (S. Sahayanathan); cdr@uoc.ac.in (C.D. Ravikumar)

ORCID(s): 0000-0000-0000-0000 (A. Thekkoth)

and/or the photon fields external to the jet (EC) [17, 18]. The ambient external photon field can be Ly- $\alpha$  line emission from broad line region (BLR) or the thermal IR emission from molecular torus. In the case of FSRQs, The X-ray emission is generally attributed to SSC, while the  $\gamma$ -ray emission is better explained by the EC process [14, 19]. Identification of the target photon field for the EC process can also provide hints about the location of the emission region in FSRQs [16, 20]. Hadronic models, on the other hand, explain the higher energy SED component as either proton synchrotron or the emission due to nuclear cascades [21, 22, 23].

Another intriguing feature of blazars is their variability patterns on timescales ranging from few minutes to days [24, 25, 26]. The availability of continuous observations from *Fermi*-LAT presents a surfeit of data to search for the shortest time variability events. The knowledge of the shortest variability time ( $\tau$ ) has been often used to constrain the emission region size and its location in blazar jets. The light crossing time suggests the emission region size,  $R$ , is less than  $c \delta \tau / (1 + z)$ , where,  $\delta$  is the relativistic Doppler factor. If the emission arises from a homogeneous region, then  $R > r_g$ , where  $r_g \sim \frac{GM}{c^2}$ , is the Schwarzschild radius of the central blackhole. If  $\psi$  is the semi aperture angle of the conical jet, then the location of emission region from the central black hole would be  $r \sim R/\psi$ . The minute timescale variability suggest a compact emission region situated at sub-parsec scales from within the broad line region [27, 28]. Conversely, for the  $\gamma$ -rays to escape from the pair production losses with the ambient photon field (BLR), the emission region should be sufficiently far from the central engine [29].

Modelling the lightcurve variability patterns as well as the spectral energy distribution (SED) are powerful tools for deciphering the underlying particle distribution and the physical processes responsible for the broadband emission. The multi-wavelength SED of 4C 31.03 during the quiescent phase has been previously modeled under hadronic scenario using proton synchrotron emission [30]. Due to the decade long quiescent phase, this source has been sparsely studied. In this paper, we performed a comprehensive study on the major  $\gamma$ -ray outbursts of 4C 31.03 using its variability patterns and multi-wavelength observations. As before mentioned, up to authors' knowledge, this is the first study reporting the variability and multi-wavelength aspects of these flaring events from 4C 31.03. The paper is organized as follows: in the next section, we provide the details of the selected observations and the data analysis procedures. In §3, we present our results and discuss the inferences drawn from our study in detail. In the last section, we conclude our findings. Throughout this work, we used the cosmology with  $\Omega_m = 0.3$ ,  $\Omega_\lambda = 0.7$  and  $H_0 = 70 \text{ km s}^{-1} \text{ Mpc}^{-1}$ .

## 2. Multiwavelength Observations and Data Reduction

### 2.1. $\gamma$ -ray Observations

The *Fermi*-LAT observation in the energy range 0.1-500 GeV spanning the time interval 2009 - 2023 (MJD

54830-60160) has been used in this work to study the  $\gamma$ -ray emission of 4C 31.03. The region of interest (ROI) selected for this analysis was a 10 degree circular region centered at RA=18.2227 and DEC=32.1399. We used the software package *Fermitools* version 2.2.0 for data reduction and analysis. The photon events were filtered and extracted the good time intervals (GTI) following standard criteria mentioned in <sup>1</sup>. The livetime cube and exposure map have been generated using '*gtlcube*' and '*gtxpmap*' tools. A circular region of radius 25 degree centered at the target has been selected as the source region and exposure map is generated for the same. We have optimized the ROI of all the sources of interest with models from the 4FGL catalog. An initial sky model for all the sources of interest has been obtained after performing a binned likelihood analysis over the total observation. The parameters of the sources within the ROI have been kept free while that of the other sources were frozen to their catalog value. We have also applied a selection, based on the value of test statistics, TS, such that the parameters of all sources for which TS (in the entire time interval)  $< 9$  were kept fixed. The sky model thus acquired has been used in the preparation of lightcurves and the  $\gamma$ -ray SEDs. We have generated a 7 day binned global light curve of 4C 31.03 for the entire observation. The  $\gamma$ -ray lightcurves during the recent active phase were obtained with two time bin sizes, 0.5 and 1 day binning. We adopted the unbinned likelihood analysis for obtaining the light curves. The PowerLaw2 function was chosen to model the  $\gamma$ -ray spectrum of 4C 31.03 while generating the lightcurves. In order to obtain the fit convergence in each time bin, we made an iterative procedure: initially, the 'DRMNF' optimizer was applied to fit in the individual time bins and whenever this fit failed to converge, we deleted all the sources with TS  $< 5$ . In the final step, we performed the fit within all time bins after setting 'Newminuit' as the optimizer.

### 2.2. *Swift* Observations

The *Swift* telescope has also monitored 4C 31.03 simultaneously with the recent outburst in the X-ray and optical/UV bands. To study the X-ray spectrum, we obtained the ready-to-use *Swift*-XRT spectra from the automated online tool *Swift*-XRT data products' generator [31]. This tool automatically selects the source and background regions based on count rate and also performs the corrections for pile up and bad pixels. All the spectra were rebinned to 20 minimum counts in each energy bin using ftool '*grppha*'. Then the spectra were loaded and fitted in the X-ray fitting platform XSPEC [32]. The unabsorbed fluxes in the selected energy bins were estimated after setting the value of hydrogen column density to  $n_H = 7.8 \times 10^{20} \text{ cm}^{-2}$  [33]. We have also obtained the values of the photon indices and the unabsorbed integrated fluxes in the energy range 0.3-10 keV for each observation.

The UVOT observations were downloaded from the archive and reduced following standard procedures <sup>2</sup>. The

<sup>1</sup><https://fermi.gsfc.nasa.gov/ssc/data/analysis>

<sup>2</sup><https://swift.gsfc.nasa.gov/analysis/threads>

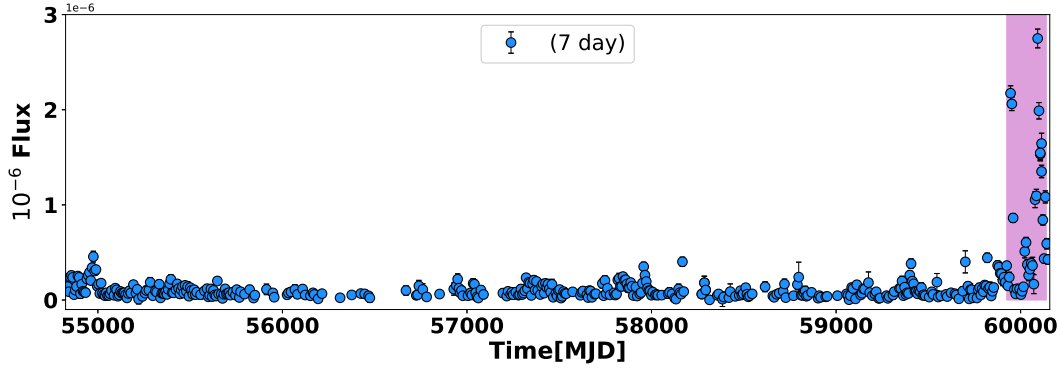


**Figure 1:** 7 day binned lightcurve of 4C 31.03 generated using *Fermi*-LAT observations spanning the time 54832-60152 MJD. The shaded time period represents the observed recent high activity epoch. The  $\gamma$ -ray fluxes are in the units of  $\text{phs cm}^{-2} \text{s}^{-1}$ .

**Table 1**

The summary of the Data analysis performed for the Swift XRT and UVOT observations.

Swift-XRT						
state	Flux ( $\text{ergs cm}^{-2} \text{s}^{-1}$ )	Photon Index ( $\Gamma/\alpha$ )	Curvature ( $\beta$ )	$\chi^2/\text{Dof}$		
Flare1	$(3.6 \pm 0.3) \times 10^{-11}$	$2.8 \pm 0.2$	$-0.6 \pm 0.1$	58.5/80		
Flare2	$(1.5 \pm 0.1) \times 10^{-11}$	$1.4 \pm 0.07$	-	45.7/49		
Quiescent	$(5.6 \pm 0.4) \times 10^{-12}$	$1.5 \pm 0.1$	-	42/35		
Swift-UVOT (Fluxes in $\text{phs cm}^{-2} \text{s}^{-1}$ )						
	V	B	U	UVW1	UVM2	UVW2
Flare1	$3.8 \pm 0.3$	$4.8 \pm 0.3$	$3.7 \pm 0.3$	$3.0 \pm 0.2$	$2.1 \pm 0.1$	$2.6 \pm 0.2$
Flare2	$3.0 \pm 0.07$	$3.7 \pm 0.06$	$2.6 \pm 0.05$	$1.96 \pm 0.04$	$1.3 \pm 0.03$	$1.5 \pm 0.02$
Quiescent	$0.37 \pm 0.01$	$0.43 \pm 0.01$	$0.29 \pm 0.01$	$0.23 \pm 0.01$	$0.18 \pm 0.01$	$0.20 \pm 0.005$

images in all the available filters were summed over the extensions using the tool *uvotimsum*. A circular region of radius 6 arcsec was used to extract the source counts, while a 20 arcsec radius circle in the source free region was used for background estimation. For all observations, we also produced spectral products using the tool *uvot2pha* and these were fitted in XSPEC to estimate the total integrated flux in the energy range 2-7 eV. All the fluxes in each filter as well as the integrated fluxes were corrected for galactic absorption by fixing  $E(B-V)=0.0503$  for  $R_V=3.1$  [34]. The results of the data reduction and analysis of *Swift* observations are presented in Table 1.

### 3. RESULTS AND DISCUSSION

#### 3.1. $\gamma$ -ray temporal analysis of 4C 31.03

In Figure 1, we show the 7-day binned  $\gamma$ -ray lightcurve obtained for the time duration 54832-60152 MJD. It is evident from the figure that the source 4C 31.03 has shown such pronounced activity (shaded region) for the first time since its discovery. In this work, we imposed two conditions on all the lightcurves studied, which are : 1) In each time bin, test statistics,  $TS \geq 4$  and 2) uncertainty in flux,  $\Delta F \leq 0.5 F$ . There are two reported instances during which the flux exhibited an extraordinary increase [1, 6]. In order to achieve better resolution in time and to differentiate the rise and decay substructures in this unprecedented high activity period, we obtained a 1 day as well as 12 hour binned lightcurves during the shaded region in Figure 1. The highest flux obtained is  $4.8 \times 10^{-6} \text{ phs cm}^{-2} \text{ s}^{-1}$  for one day binned and

**Table 2**

The duration and peak times of the flares identified.

Flare	$T_{\text{start}}$ MJD	$T_{\text{peak}}$ MJD	$T_{\text{stop}}$ MJD
1	59945.0	59948.0	59952.0
2	59953.0	59955.5	59960.0
3	60031.0	60032.0	60033.0
4	60071.0	60095.0	60123.0
5	60131.5	60134.7	60138.0

$6.9 \times 10^{-6} \text{ phs cm}^{-2} \text{ s}^{-1}$  for 12 hour binned lightcurve. To have a systematic identification of the duration of flares, we employed an algorithm which was used in previous studies [35, 36]. This algorithm utilizes Bayesian blocks and starts by identifying a block with higher flux than its preceding and succeeding blocks. It then proceeds in both directions from the peak, as long as sequentially lower blocks are found. The start/end of a flare is set by the flux exceeding/falling under a predefined flux level (average flux). This approach is referred to as the "HOP algorithm," and was first introduced by [37]. We identified five epochs of flaring in the 12 hour and 1 day binned lightcurves shown as the shaded regions in Figure 2. The top 2 panels display the 12 hour and one day binned lightcurves along with the Bayesian blocks respectively. In the bottom panel, we plotted the  $\gamma$ -ray photon index,  $\Gamma_\gamma$ , obtained from the 1 day binned lightcurve. It is apparent from the figure that  $\gamma$ -ray spectrum shows a clear hardness during the flares. Out of all the identified flares, 3 time

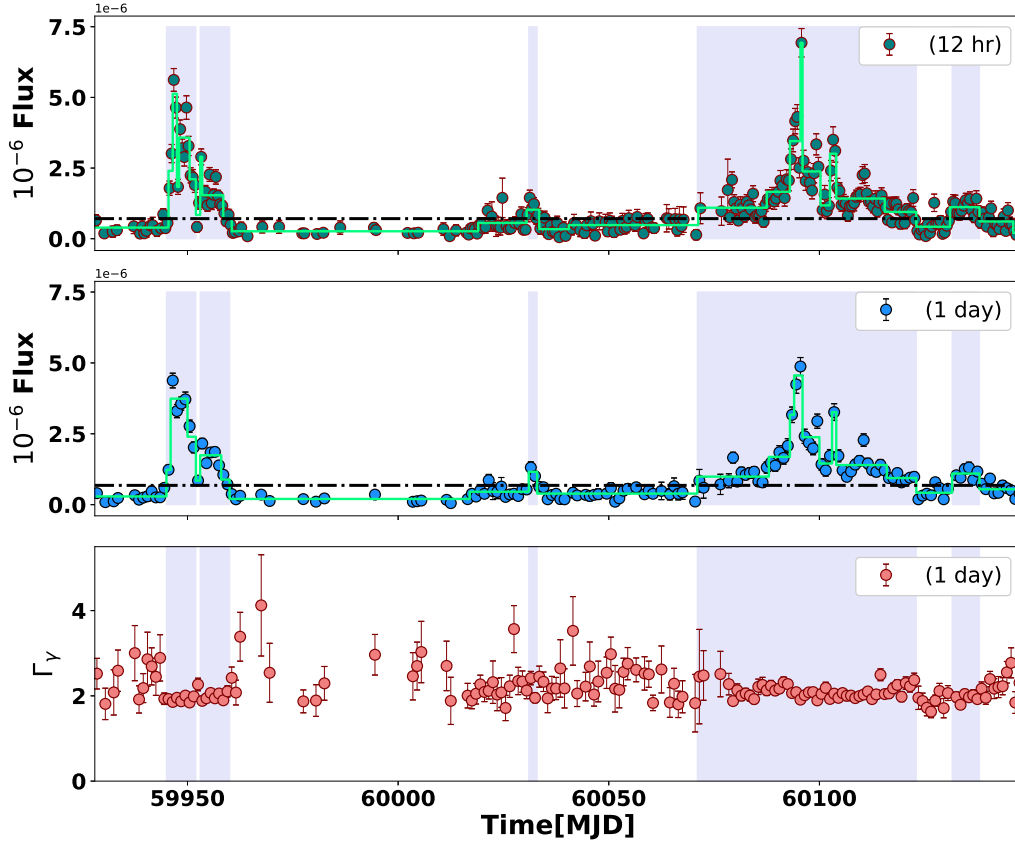


**Figure 2:** *Fermi*  $\gamma$ -ray lightcurve of 4C 31.03 spanning the time 59940-60152 MJD. Top two panels show the 12 hour and 1 day binned lightcurves. Fluxes are in units of phs  $\text{cm}^2 \text{s}^{-1}$ . The solid line indicate the Bayesian blocks obtained while horizontal dashed line represents the average flux level. In the bottom panel, the photon index obtained from 1 day binned lightcurve has been plotted. The shaded time periods represent the duration of flares as characterized from the HOP analysis.

intervals (flares 1,2, and 4) corresponding to MJD 59945-59952, 59953-59960, and 60071-60123, show prominent activity. The other 2 epochs exhibit less significant activity, especially flare 3. The time periods corresponding to the beginning and the decay of flares as well as the period of maximum flux, are tabulated in Table 2. The Bayesian blocks and the HOP groups in this analysis were obtained using an open source python module provided by Wagner et al. [36]. Furthermore, the variation of  $\Gamma_\gamma$  around 2 during the flares hints that the external Compton peak falls in the *Fermi* energy range ( $> 100 \text{ MeV}$ ).

### 3.1.1. Searching for the fastest $\gamma$ -ray variability

To investigate the fastest flux doubling or halving time during the flares, we scanned the 12 hour binned lightcurve using the equation:

$$F(t) = F(t_0) 2^{-(t-t_0)/\tau} \quad (1)$$

where  $F(t)$  and  $F(t_0)$  are the fluxes at consecutive times  $t$  and  $t_0$  respectively and  $\tau$  is the characteristic time scale. We further imposed a minimum  $3\sigma$  significance level for the difference in flux at consecutive times [38] for this analysis. The values of  $\tau$  corresponding to the times at which the above condition has been satisfied are shown in Table 3.

Our analysis shows variability time scales ranging from 5 to 18 hours, with the fastest flux decay between MJD 59951-59952 in a time scale of  $5.5 \pm 0.7$  hours. Following the light travel arguments discussed in §1, the size of the emission region,  $R$  for a  $\tau$  in the order of hours, will be roughly in the range  $10^{15} - 10^{16} \text{ cm}$  [39, 20]. An observed hour scale flux variability time usually indicates further shorter cooling time scale for the emitting particle distribution. And it is worth mentioning that a cooling time scale lesser than one hour supports the BLR while more than 10 hour suggests the molecular torus as the emission location in blazars [40]. Additionally, we performed a  $\chi^2$  minimization fitting of the rise and decay subflares using exponential profiles represented by

$$F(t) = 2F_0 \left[ \exp\left(\frac{t_0 - t}{T_r}\right) + \exp\left(\frac{t - t_0}{T_d}\right) \right]^{-1} \quad (2)$$

where  $T_r$  and  $T_d$  are the rise and decay times of subflares, respectively, and  $F_0$  is the approximated amplitude of each subflare, measured at time  $t_0$ . We considered the epochs 59945-59960 and 60071-60123 including the three prominent flares 1,2 and 4 as given in Table 2. All the fluxes were estimated above a constant base flux in the analysis. The plots of the flares with the total best fit function are shown in

**Table 3**

The summary of the variability times found.  $t_0$  and  $t_1$  are the times in MJD;  $F(t_0)$  and  $F(t_1)$  are the fluxes in units of ( $\times 10^{-6}$ ) phs  $\text{cm}^{-2} \text{s}^{-1}$ ; significance of difference in flux in  $\sigma$ ; variability time scale ( $\tau$ ); uncertainty in  $\tau$ ; Rise or Decay.

$t_0$	$t_1$	$F(t_0)$	$F(t_1)$	Significance	$\tau$ (hour)	$\Delta\tau$ (hour)	R/D
59945.25	59945.75	$0.6 \pm 0.2$	$1.8 \pm 0.3$	3.8	7.2	1	R
59945.75	59946.25	$1.8 \pm 0.2$	$3 \pm 0.3$	3.0	16	0.6	R
59946.25	59946.75	$3 \pm 0.3$	$5.6 \pm 0.4$	5.1	13	0.5	R
59947.25	59947.75	$4.6 \pm 0.4$	$1.8 \pm 0.3$	6.1	9	0.6	D
59947.75	59948.25	$1.8 \pm 0.3$	$3.9 \pm 0.3$	4.9	11	0.6	R
59949.25	59949.75	$2.9 \pm 0.3$	$4.6 \pm 0.4$	3.3	17.6	0.5	R
59951.75	59952.25	$1.9 \pm 0.2$	$0.41 \pm 0.08$	4.7	5.5	0.7	D
59952.75	59953.25	$1.3 \pm 0.2$	$3 \pm 0.3$	4.5	10	0.7	R
59953.25	59953.75	$2.9 \pm 0.3$	$1.4 \pm 0.2$	4.3	11	0.7	D
59954.75	59955.25	$1.2 \pm 0.2$	$2.3 \pm 0.2$	3.4	13	0.7	R
59955.25	59955.75	$2.3 \pm 0.2$	$1.3 \pm 0.2$	3.0	14	0.8	D
60078.75	60079.25	$0.8 \pm 0.2$	$2.1 \pm 0.3$	3.6	8.2	1	R
60094.75	60095.25	$4.3 \pm 0.4$	$2.5 \pm 0.3$	3.2	15.4	0.6	D
60095.25	60095.75	$2.5 \pm 0.3$	$7 \pm 0.5$	7.2	8.2	0.6	R
60095.75	60096.25	$7 \pm 0.50$	$2.8 \pm 0.4$	6.7	9	0.5	D
60099.75	60100.75	$2.5 \pm 0.3$	$1 \pm 0.2$	3.7	18	2	D

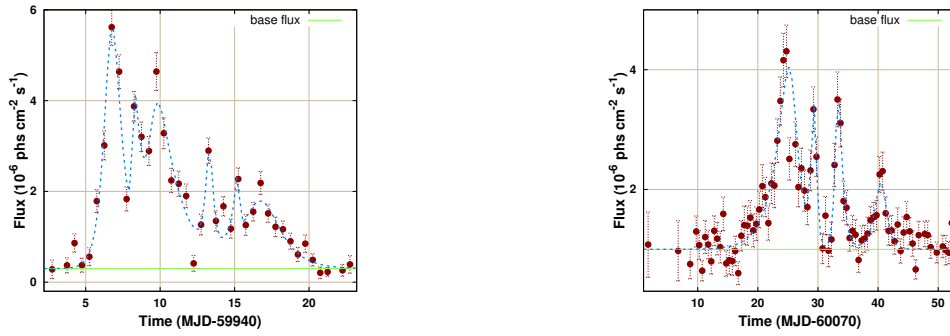


**Figure 3:** Plots showing the temporal profile fitting of the 3 prominent flares observed. The dashed curve represent the total best fit model and solid line is the base flux level chosen. Flare 1 and 2 fitted together (left). Flare 4 is plotted in the right panel.

Figure 3. Certain sub-flares within the flare 1 and 2 contain only three data points and cannot be fitted with the equation 2. Hence the parameters of these subflares (2,4, and 5) were kept fixed at their optimized values. These fixed parameters are given in Table 4 with suffix \*. For the sub-flares with more than three data points we quote the standard errors. We also found the value of asymmetry  $\zeta$  for each subflare from the expression,  $(T_r - T_d)/(T_r + T_d)$ . The flares with  $\zeta < 0$  are known as fast rise and exponential decay (FRED) flares which are common in  $\gamma$ -ray lightcurves. Such flares support the scenario of an injection time scale faster than the radiative time scale [35]. However, in our analysis, very few sub-flares are found with  $\zeta < 0$ . Moreover, most of the sub-flares are slightly/moderately asymmetric since  $|\zeta| < 0.7$  [24].

### 3.1.2. High and low-energy $\gamma$ -ray lightcurves

The good test statistics for the fluxes during the 3 prominent flares made it possible to split the lightcurve into low-energy (0.1-1 GeV) and high-energy (1-500 GeV) divisions. In Figure 4, we show the lightcurves in these energy ranges plotted together (scaled appropriately). In the bottom panel, we plotted the hardness ratio (HR) defined by,

$$HR = \frac{f_H - f_L}{f_H + f_L}$$

where  $f_H$  and  $f_L$  are the fluxes in the high and low energy bands respectively. The nature of variations in the low and high energy scenarios seems similar, however, during most of the epochs, the flaring is more intense in the low energy regime. This observation indicates that the recent active phase of 4C 31.03 is primarily caused by the low energy electrons in the particle spectrum. We also explored the time lag between the low and high energy  $\gamma$ -ray lightcurves using the Discrete Correlation Function (DCF) [41]. A zero time-lag between these lightcurves is obtained and this may suggest an energy-independent evolution of the light curves or the underlying electron distribution. However, the cooling timescales of the emitting electron distribution at these photon energies are too short than the 12 hour binned light curve used for the DCF analysis. For instance, the cooling time scale (equation 7 from §3.3) corresponding to  $\sim 0.5$  GeV emission is  $\sim 7.3$  hours and the in case of  $\sim 20$  GeV it is  $\sim 1$  hour. Hence, the zero time-lag obtained through the DCF analysis indicates its inability to probe the energy-dependence of the lightcurves obtained with 12 hour binning.

### 3.1.3. $\gamma$ -ray spectral variations

In order to study the  $\gamma$ -ray spectral transitions during the recent activity phase of 4C 31.03, we obtained the corresponding SEDs for the flares 1,2,4, and 5 (§3.1) using the

**Table 4**

The rise and decay times estimated from Equation 2 for all the subflares. The peak flux  $F_0$  is in units of ( $\times 10^{-6}$ ) phs  $\text{cm}^{-2} \text{s}^{-1}$ .

$t_0$ (MJD)	$F_0$	$T_r$ (day)	$T_d$ (day)	$\zeta$
Flare 1& 2:		$\chi_{\text{red}}^2=1.21$	dof=28	
59946.75	$5.2 \pm 0.4$	$0.43 \pm 0.04$	$0.59 \pm 0.06$	0.17
59948.20	$2.3^*$	$0.1^*$	$0.5^*$	-0.7
59949.50	$2.9 \pm 0.3$	$0.37 \pm 0.08$	$1.4 \pm 0.2$	0.59
59953.25	$2.1^*$	$0.21^*$	$0.22^*$	0.02
59955.50	$1.0^*$	$0.34^*$	$0.06^*$	0.7
59956.75	$1.5 \pm 0.2$	$1.2 \pm 0.3$	$1.2 \pm 0.2$	0.001
Flare 4:		$\chi_{\text{red}}^2=1.8$	dof=48	
60095.75	$3.8 \pm 0.3$	$2.2 \pm 0.3$	$0.91 \pm 0.2$	-0.42
60099.50	$2.2 \pm 0.5$	$0.55 \pm 0.2$	$0.30 \pm 0.1$	-0.31
60103.25	$2.5 \pm 0.5$	$0.40 \pm 0.1$	$0.64 \pm 0.1$	0.26
60110.50	$1.1 \pm 0.3$	$1.0 \pm 0.3$	$0.75 \pm 0.3$	-0.14

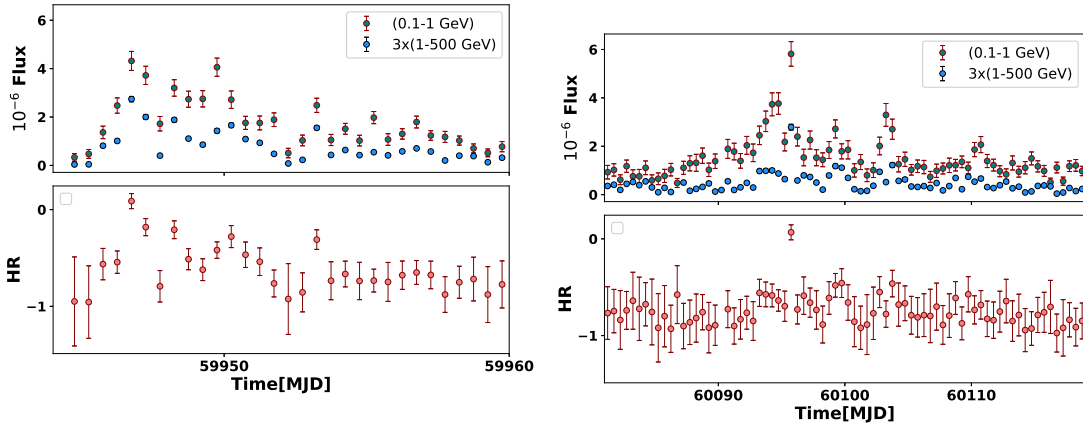


**Figure 4:** The  $\gamma$ -ray lightcurves with 12 hour binning in the low (0.1-1 GeV) and high-energy (1-500 GeV) ranges are shown in the top panels. The high-energy light curve has been scaled to plot together. In the bottom panel, hardness ratio  $HR$  has been plotted against time. Left) Flare 1 and 2 combined. Right) Flare 4.

*likeSED.py* module. The SED for flare 3 cannot be constrained due to low photon statistics. We also extracted the  $\gamma$ -ray SED during the epoch 59960-59975, when the source is at a quiescent state. This SED is used later to compare the broadband SEDs during different activity states of the

source (§3.3). The SEDs corresponding to these epochs were fitted using power-law (PL), log-parabola (LP), broken power-law (BPL), and power-law with an exponential cutoff (PLEC) models. The PL model was able to give an

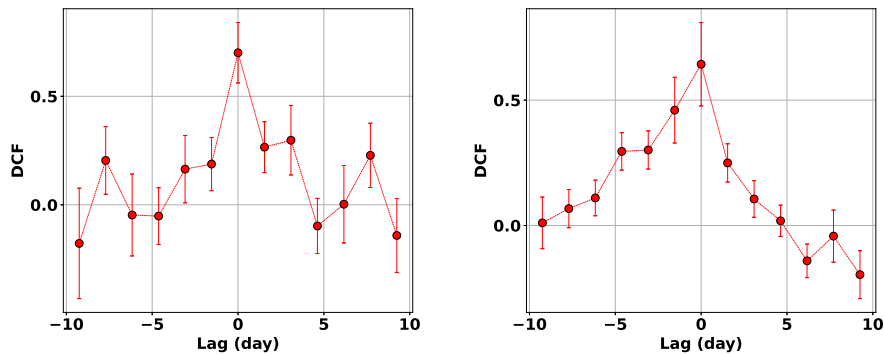


**Figure 5:** DCF is plotted across the lag in days measured as Time(100-500 GeV) - Time(0.1-100 GeV) lightcurves. Left) DCF corresponding to flare 1 and 2 combined. Right) DCF obtained during flare 4.

acceptable fit only during the quiescent state. The significance of curvature/break, ( $TS_{\text{curv}}$ ) of a spectrum can be estimated as TS (model of curvature/break) - TS (Power-law). According to this criterion, a spectrum shows significant curvature/break if  $TS_{\text{curv}} \geq 16$ , as it indicates a  $4\sigma$  level confidence [42, 43]. The results of this analysis with the  $TS_{\text{curv}}$  values obtained are given in Table 5. The  $TS_{\text{curv}}$  results show that nearly all the flaring  $\gamma$ -ray spectra (flares 1, 2, and 4) exhibit a notable break, as BPL model has been found to give better statistics in these cases. However, in the case of flares 1 and 4, the  $\gamma$ -ray spectra can also be well described by LP and PLEC models in addition to BPL (Table 5). In the case of flare 5, the results show that the spectrum can be described equally well by all the models. The plots of the  $\gamma$ -ray SEDs obtained along with the models are shown in Figure 6.

The break in the spectra is found to be almost stationary and lies around 2 GeV. The GeV spectral break in *Fermi* bright blazars might be intrinsic in nature and can be attributed to the shape of the underlying particle distribution or the target photon spectrum [44, 45]. The break/curvature in the  $\gamma$ -ray spectrum can also be caused by the pair absorption of GeV photons by the Ly- $\alpha$  line emission of the BLR. This will be the case only when the emission region lies within the BLR [46]. However, a recent study by Costamante et al. [47], investigated the external Compton scenario involving BLR photons in a sample of 106 *Fermi* bright FSRQs (including 4C 31.03) suggests that the  $\gamma$ -ray spectra of such sources do not exhibit significant absorption effects. Instead,  $\gamma$ -rays seems to be produced outside the BLR.

### 3.1.4. Highest photon energy

As mentioned above, the detection of photons with energy greater than 20 GeV is pivotal in the case of FSRQ type sources since the photons of such energy detected can plausibly indicate that the  $\gamma$ -ray production happens beyond the BLR [48, 47]. We found the energies of the photons detected during the active state of 4C 31.03 which are positionally consistent with the source co-ordinates using the fermitool *gtsrcprob*. Three epochs were noticed at which photons with energy greater than 50 GeV have been detected from the source with more than 99% association probability. They are 51.3 GeV at 59946.76 MJD, 82.6 GeV at 59947.15 MJD, and 65.5 GeV at 60107.24 MJD.

### 3.2. Constraints on the Doppler factor

The detection of  $\gamma$ -rays from blazars has been used to constrain various source parameters [38, 26]. The observed variability timescale ( $\tau$ ) coupled with the light travel time arguments can effectively constrain the emission region size as

$$R \leq \frac{c\tau}{1+z} \delta \quad (3)$$

where  $\delta$  is the jet Doppler factor. Using this relation along with the pair production opacity of the  $\gamma$ -ray photons against the target X-ray photons, one can obtain a lower limit on the jet Doppler factor [29, 24]. For a  $\gamma$ -ray photon of energy  $\epsilon$  in

$m_e c^2$  units and the target X-ray photon flux  $f_x$ , the minimum jet Doppler factor can be deduced as

$$\delta \geq \left[ \frac{\sigma_T d_L^2 (1+z)^2 f_x \epsilon}{4\tau m_e c^4} \right]^{\frac{1}{6}} \quad (4)$$

where,  $\sigma_T$  is the Thomson scattering cross section and  $d_L$  is the luminosity distance. The highest photon energy detected during the time period of flares 1 and 2 is 82.6 GeV (§3.1.4) and the X-ray flux obtained in the energy range 0.3-10 keV during the flaring state is  $2.915 \times 10^{-11}$  erg/cm<sup>2</sup>/s. Incorporating this values with shortest variability timescale of 5.5 hours (§3.1.1) in the above equation, we found the minimum jet Doppler factor during the flaring state as 17. Using this value in equation 3, the upper-limit on the emission region size  $R$  is estimated to be  $\sim 10^{16}$  cm. For a similar value of the emission region size and the target X-ray photon flux  $5.6 \times 10^{-12}$  erg/cm<sup>2</sup>/s, corresponding to the quiescent state, the jet Doppler was found to be 13. Here, we have used the highest photon energy as 26 GeV (detected during the quiescent state on 59960 MJD).

### 3.3. Broadband SED analysis

The broadband spectral modeling of the source with different emission processes can provide clues on the gamma-ray emission mechanism and the plausible location of the emission region in the blazar jet [39, 13]. For this, we selected three epochs from the multi-wavelength light curve corresponding to two high activity states and a quiescent state. These epochs were also chosen based on the availability of the *Swift* observations and the selected time windows are shown in Figure 7. In Figure 8, we show the observed SED corresponding to these flux states.

The broadband SEDs available at optical/UV, X-ray, and  $\gamma$ -rays from the *Swift*-XRT and *Fermi* observations are modeled using a one-zone leptonic model considering synchrotron, SSC, and EC processes [19, 49]. This model assumes the emission region to be a sphere of radius  $R$  moving down the blazar jet with the bulk Lorentz factor  $\Gamma$  and at an angle  $\theta$  with respect to the observer. The emission region is populated with a non-thermal electron distribution represented by a broken power-law,

$$N(\gamma) d\gamma = \begin{cases} K \gamma^{-p} d\gamma & \text{for } \gamma_{\min} < \gamma < \gamma_b \\ K \gamma_b^{q-p} \gamma^{-q} d\gamma & \text{for } \gamma_b < \gamma < \gamma_{\max} \end{cases} \quad (5)$$

where,  $\gamma$  is the dimensionless energy of the electron and,  $p$  and  $q$  are the low and high-energy indices of the distribution with  $\gamma_b$  as the break energy. The magnetic field responsible for the synchrotron emission is assumed to be tangled, and the external photon fields for the EC process are the dominant Ly- $\alpha$  emission from the BLR and the thermal IR photons from the molecular torus. Due to relativistic motion, the emitted source radiation will be blue-shifted and boosted in the observer's frame by the Doppler factor  $\delta$ .

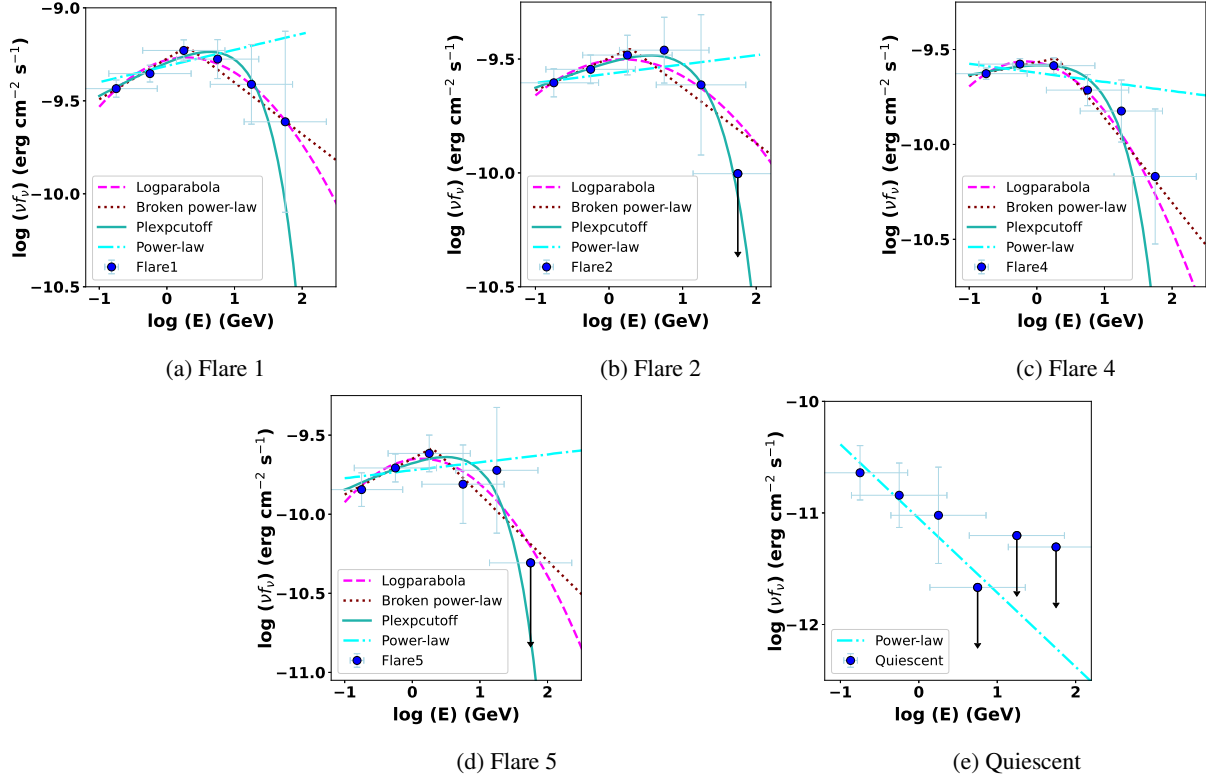


**Figure 6:** Plots showing the  $\gamma$ -ray SEDs during different activity states along with the fitted spectral models. The details of models are inboxed in the plots.

**Table 5**

Results of  $\gamma$ -ray SED analysis for various observed states.

Flare group/ states	$F_{0.1-300\text{GeV}}$ ( $10^{-6}$ ph $\text{cm}^{-2}$ $\text{s}^{-1}$ )	PowerLaw $\Gamma$			TS	TS <sub>curv</sub>
1	$2.6 \pm 0.08$	$-1.9 \pm 0.02$	–	–	6682.16	–
2	$1.7 \pm 0.07$	$-2.0 \pm 0.03$	–	–	3116.97	–
4	$1.6 \pm 0.03$	$-2.0 \pm 0.02$	–	–	12894.82	–
5	$1.1 \pm 0.07$	$-1.9 \pm 0.04$	–	–	1464.99	–
Quiescent	$0.16 \pm 0.02$	$-2.7 \pm 0.2$	–	–	109.53	–
LogParabola						
		$\alpha$	$\beta$			
1	$2.4 \pm 0.08$	$1.8 \pm 0.03$	$0.07 \pm 0.01$	–	6736.82	54.66
2	$1.6 \pm 0.07$	$1.9 \pm 0.04$	$0.05 \pm 0.02$	–	3125.17	8.19
4	$1.5 \pm 0.03$	$1.9 \pm 0.02$	$0.08 \pm 0.01$	–	13003.37	108.55
5	$1.0 \pm 0.07$	$1.8 \pm 0.07$	$0.09 \pm 0.03$	–	1468.75	4.75
Broken PowerLaw						
		$\Gamma_1$	$\Gamma_2$	$E_{\text{break}}$ (GeV)		
1	$2.5 \pm 0.08$	$-1.8 \pm 0.03$	$-2.3 \pm 0.07$	$2.0 \pm 0.05$	6725.74	43.58
2	$1.6 \pm 0.07$	$-1.9 \pm 0.04$	$-2.2 \pm 0.1$	$2.0 \pm 0.07$	3134.50	17.53
4	$1.5 \pm 0.03$	$-1.9 \pm 0.02$	$-2.4 \pm 0.06$	$1.8 \pm 0.2$	12965.38	70.56
5	$1.0 \pm 0.07$	$-1.8 \pm 0.07$	$-2.4 \pm 0.2$	$2.0 \pm 0.03$	1478.32	13.41
PLExpCutoff						
		$\Gamma_{\text{plec}}$		$E_{\text{cutoff}}$ (GeV)		
1	$2.5 \pm 0.08$	$-1.8 \pm 0.03$	–	$22.0 \pm 5.0$	6733.48	51.32
2	$1.6 \pm 0.07$	$-1.9 \pm 0.03$	–	$30.0 \pm 0.8$	3110.54	-6.43
4	$1.5 \pm 0.03$	$-1.9 \pm 0.02$	–	$16.0 \pm 3.0$	12915.87	21.07
5	$1.0 \pm 0.07$	$-1.8 \pm 0.07$	–	$16.5 \pm 7.4$	1461.22	-3.68

The emissivity functions corresponding to these radiative processes are solved numerically and the routines developed are incorporated as a local model in the spectral fitting package *XSpec* [32]. For numerical simplicity, the line emission from BLR is treated as a blackbody at a temperature of 42000K, such that the peak frequency is equivalent to that of the Ly- $\alpha$  emission line ( $2.47 \times 10^{15}$  Hz). The emission

from the molecular torus is assumed to be a blackbody at a temperature of 1000K. The energy density of the target photon field involved in the external Compton scattering process is expressed as a fraction ( $f$ ) of the corresponding black-body energy density.

$$U_{\text{target}} = f \times U_{\text{BB}} \quad (6)$$



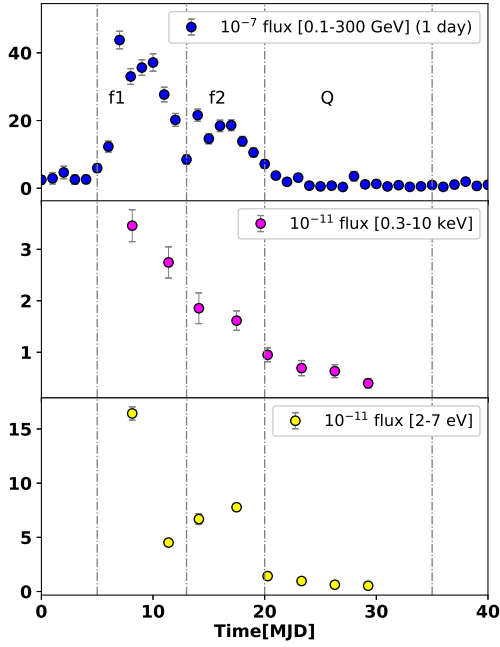


**Figure 7:** Multi-wavelength lightcurve of 4C 31.03 from MJD 59940-59965. Top panel shows the  $\gamma$ -ray flux, middle the X-ray flux and bottom panel optical/UV flux. The middle and bottom panel fluxes are in units of  $\text{erg cm}^{-2} \text{s}^{-1}$ .  $\gamma$ -ray flux is in unit of  $\text{phs cm}^{-2} \text{s}^{-1}$ .

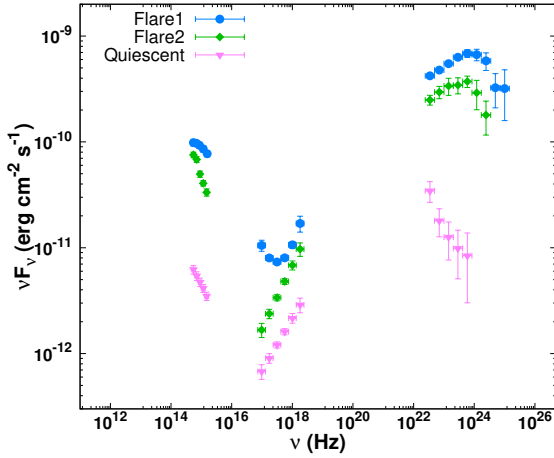


**Figure 8:** Plot showing all the 3 multiwavelength SEDs together.

where,  $U_{\text{BB}} = \frac{4\sigma_B}{c}T^4$  is the black-body energy density. The total number of parameters governing the broadband spectrum exceeds the information available from the optical, X-ray, and  $\gamma$ -ray energies, and hence, certain constraints were imposed. We assumed near equi-partition between the magnetic field and particle energy densities [50, 51]. This is defined as a parameter  $\eta$  which is the ratio between particle

to magnetic field energy densities. The emission region size was initially kept free, and then optimized at  $2 \times 10^{16}$  cm. Besides these, we also kept the parameters  $\gamma_{\text{min}}=10$ ,  $\gamma_{\text{max}}=2 \times 10^6$ , and viewing angle,  $\theta=2^\circ$  fixed.

The spectral fit to the different activity states using these emission processes was first performed by setting all parameters free except the ones mentioned above. However, the confidence intervals were obtained only for the parameters  $p, q, \gamma_b, B$ , and  $U_{\text{target}}$ , since the iterations were unable to converge due to plausible degeneracies. In Table 6, we provide the details of the best-fit parameters, and the spectrum corresponding to these best-fit parameters are shown in Figure 9 with the right panels showing the output from *XSpec*.

The observed fluxes at the three selected epochs were reasonably reproduced by the model using synchrotron, SSC and EC-IR emission processes. Comparing the SEDs in the Figure 8, one can note that the flux has substantially increased across all the wavebands during flares. Our SED fit results suggest that this transition is associated with significant variations in most of the source parameters, including low and high energy particle indices, bulk Lorentz factor,  $\gamma_b$ , magnetic field  $B$ , and the target photon energy density  $U_{\text{target}}$ . The variation in  $U_{\text{target}}$  across the activity states can be associated with the location of the emission region from the central black-hole [39]. The target photon energy density is higher for the flaring states compared to quiescent period, and this implies that during the flares, the emission region is more closer to central black-hole than in the case of quiescent state. Similarly, the energy density for Flare 1 is larger than Flare 2, suggesting the location of the emission region may be closer to the central black hole for Flare 1. The SEDs also exhibit a significant difference in the spectral shape. For example, the X-ray spectrum during flare 1 has the contribution of synchrotron and SSC processes and shows a negative curvature, while for other epochs the X-ray emission is predominantly due to SSC process.

Our broadband analysis suggests that the  $\gamma$ -ray emission from 4C 31.03 can be due to the inverse Compton scattering of IR photons from the torus. This is consistent with our findings from the  $\gamma$ -ray observational results mentioned in previous sections. Further, the observed cooling time scale of the underlying electron distribution for the EC emission can be calculated as [26, 52],

$$t_c^{\text{obs}} = \frac{3m_e c}{4\sigma_T U'} \left( \frac{v_{\text{seed}}^{\text{obs}} \Gamma(1+z)}{v_{\text{IC}}^{\text{obs}} \delta} \right)^{\frac{1}{2}} \quad (7)$$

where,  $U'$  ( $U_{\text{target}} \Gamma^2$ ) is the target photon field energy density in the co-moving frame,  $v_{\text{seed}}^{\text{obs}}$  ( $2 \times 10^{13}$ Hz) is the observed seed photon frequency (for torus IR as the target photon field) and  $v_{\text{IC}}^{\text{obs}}$  is the observed EC peak frequency. The peak EC frequency is obtained from the best-fit values of the log-parabola spectral fit to the  $\gamma$ -ray observations [53]. In the case of flare 1,  $v_{\text{IC}}^{\text{obs}}$  is equal to  $1.2 \times 10^{23}$  Hz and using the best-fit values provided in Table 6, we obtained  $t_c^{\text{obs}}$  to be 7.3

**Table 6**

Best fit values of the source parameters from broadband SED fitting.

Name of parameter	Symbol	Flare1	Flare2	Quiescent
Low energy Particle index	$p$	$2.3 \pm 0.04$	$1.8 \pm 0.05$	$1.6 \pm 0.1$
High energy Particle index	$q$	$4.4 \pm 0.1$	$4.8 \pm 0.2$	$4.2 \pm 0.1$
Break Lorentz factor	$\gamma_b$	$4542 \pm 508$	$2617 \pm 257$	$1230 \pm 69$
Magnetic Field (G)	$B$	$0.86 \pm 0.03$	$0.80 \pm 0.01$	$0.68 \pm 0.02$
Bulk Lorentz factor	$\Gamma$	28	16	13
Doppler Factor	$\delta$	28.6	24.4	21.5
Equipartition	$\eta$	3.0	3.0	3.0
External Compton Process		EC-IR	EC-IR	EC-IR
External photon energy density ( $\text{erg}/\text{cm}^3$ )	$U_{\text{target}}$	$(3.6 \pm 0.01) \times 10^{-4}$	$(2.2 \pm 0.01) \times 10^{-4}$	$(6.1 \pm 0.006) \times 10^{-5}$

hours. This is in close agreement with the decay time scales obtained from the temporal analysis of the source (§3.1.1).

### 3.4. $\gamma$ -ray flux distribution

The long-term flux variability of blazars are log-normal in nature and was reported by several authors [54, 55, 56]. The log-normal variability is generally attributed when the underlying mechanism causing variability is multiplicative in nature, with the perturbations propagating from accretion disc as an example ([57, 58]). However, the observed rapid variability in blazars supports a compact emission region which in turn demands the origin of variability to be associated with the processes happening in the jet [24, 25, 59, 60]. When the narrow-band photon spectrum from the jet is defined by a power-law, a log-normal variability can also be an outcome of normal variation of the spectral index [61, 62]. In diffusive shock acceleration, the random fluctuations in the acceleration time scale induce normal variations in index which can result a a log-normal flux distribution [56]. Further, the blazars with steeper  $\gamma$ -ray spectrum have been found to be more variable since a steeper spectrum indicates higher relative amplitude fluctuations within shorter time intervals [63]. Besides these, certain blazars also exhibit a double log-normal feature which may indicate that they are governed by two definite flux states [62, 64, 65].

Being a bright  $\gamma$ -ray source after the prolonged low activity phase, 4C 31.03 forms an ideal blazar to study the log-normal flux and spectral variations. We obtained the histograms for the logarithm of fluxes and indices from the 7 day binned long-term lightcurve. To identify whether the source depicts two flux states, we first performed the histogram study using only the prolonged quiescent phase and then repeated with the inclusion of the recent active period. The histogram analysis reveals that the long-term quiescent phase flux alone can reasonably be reproduced by a single log-normal function. Conversely, a double log-normal function gives better representation for the the total flux distribution after including the active phase. However, in the double log-normal distribution, the Gaussian component corresponding to the high flux state is significantly suppressed due to the prolonged quiescent activity. Hence, we further explored the flux distribution of the active state using histogram obtained from 12 hour binned lightcurve

(for better statistics). The active state flux distribution is well addressed by a log-normal distribution in the histogram study. The histogram study, therefore supports that the blazar 4C 31.03 is characterized by two definite flux states corresponding to its quiescent and active phases. The results of this study are given in Table 7 and the histograms with the best-fit models are shown in Figure 10.

We extended our study to understand the index variations by constructing their histograms (Figure 10(d)). Interestingly, the index distributions demanded a double Gaussian shape irrespective of the flux states. A possible reason for this could be that the observed  $\gamma$ -ray spectrum falls around the peak of the Compton component and hence the spectrum is not a simple power-law. During the different flux states the  $\gamma$ -ray peak shifts significantly and the integrated flux can be either governed by low-energy or the high-energy index.

The observed log-normal flux variability can be attributed the normal variation in the spectral index. However, we find the index distributions during the flaring and quiescent states are better represented by a double Gaussian function while the flux distributions during these states suggested a single log-normal variability. Alternatively, the observed log-normality in blazars can also be attributed to the Fermi acceleration processes in the jet [56, 66, 67]. For instance, the quiescent period of the blazar may be dominated by one type of Fermi acceleration (turbulent/shock) and at the flaring period, both could be at play [68, 69]. Consistently, the flux distribution of the total period reflects a double log-normal behavior.

To scrutinize our inference drawn from the histograms, we tested the hypothesis of normality for the distributions of  $\gamma$ -ray fluxes and indices using Anderson-Darling (AD) statistics. The test results are provided in Table 8. According to the AD test performed, the logarithmic flux distribution of the total lightcurve deviates significantly from a single Gaussian behavior. This result is consistent with conclusions drawn from the histogram study which supports a double log-normal variability. The AD test performed on the active phase flux alone supports a log-normal variability in agreement with the corresponding histogram analysis. Interestingly, the AD test for the quiescent phase suggests slight deviation from the log-normal behavior which is contrary to the conclusion drawn from the histogram study. A plausible

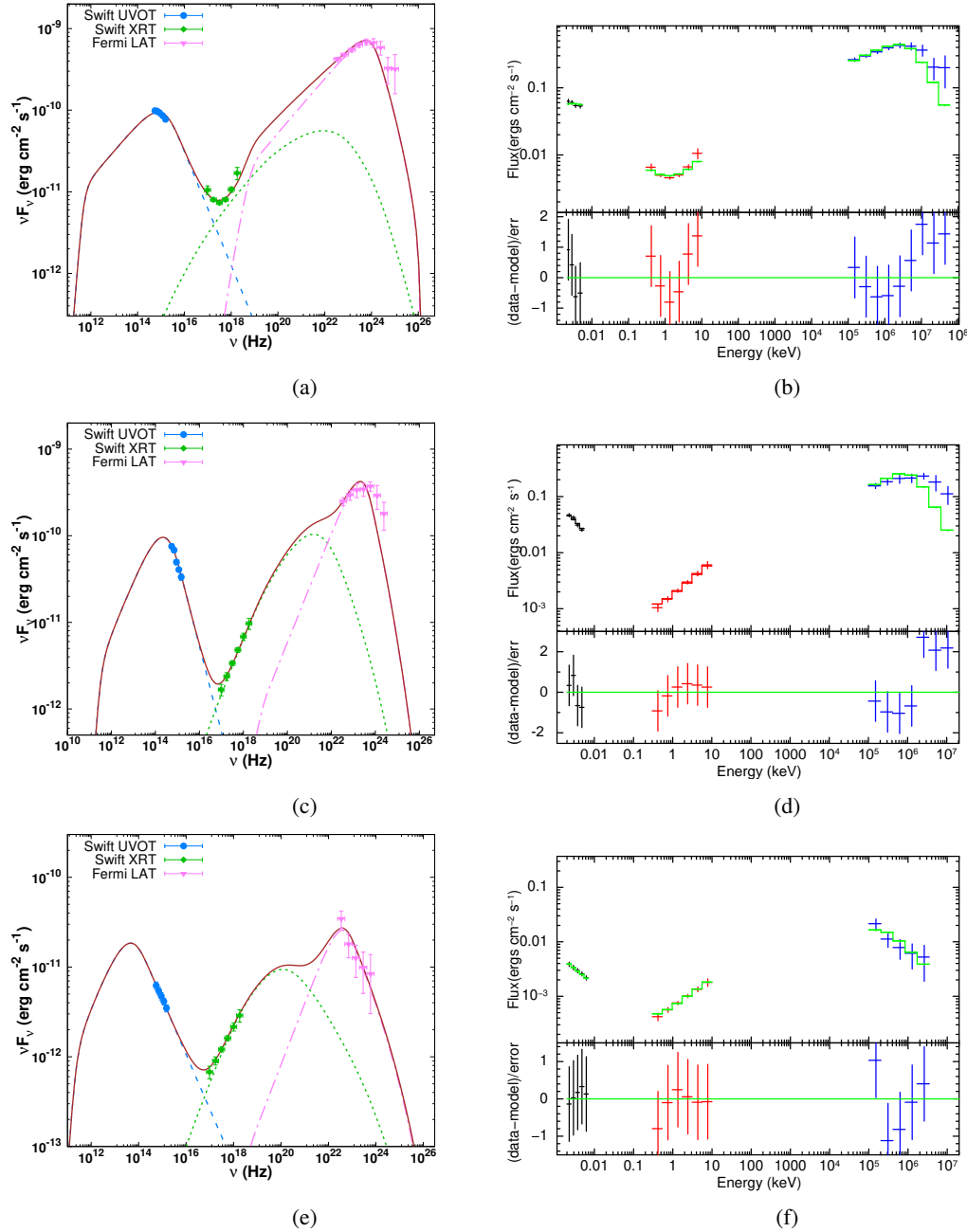


**Figure 9:** Broadband SEDs along with best-fit models (left: a) flare 1, c) flare 2, and e) quiescent state. Right panels show the corresponding *Xspec* plots showing the fit. In the left panels, dashed lines represents the synchrotron, dotted line represents the SSC and dotted dashed line the EC processes. The solid curve shows the total best-fit model.

reason could be, the quiescent period may also contain minor flares associated with different physical processes. The presence of such flares deviate the variability behavior from log-normal in case of AD test. However, in case of histogram study, these minor flares may be over shadowed by the prolonged quiescent phase and hence suggest a log-normal variability.

#### 4. Summary

The blazar 4C 31.03 has recently been reported by *Fermi*-LAT for exhibiting an exceptionally high  $\gamma$ -ray activity for the first time. In this paper, we performed a detailed study of this major outburst through temporal and spectral analysis. We used publicly available observations by *Fermi*-LAT, *Swift*-XRT, and UVOT instruments for this study.

We performed the temporal study after obtaining  $\gamma$ -ray lightcurves with 7 day, 1 day, and 12 hour binning. Through the statistical analysis of lightcurves using Bayesian blocks,

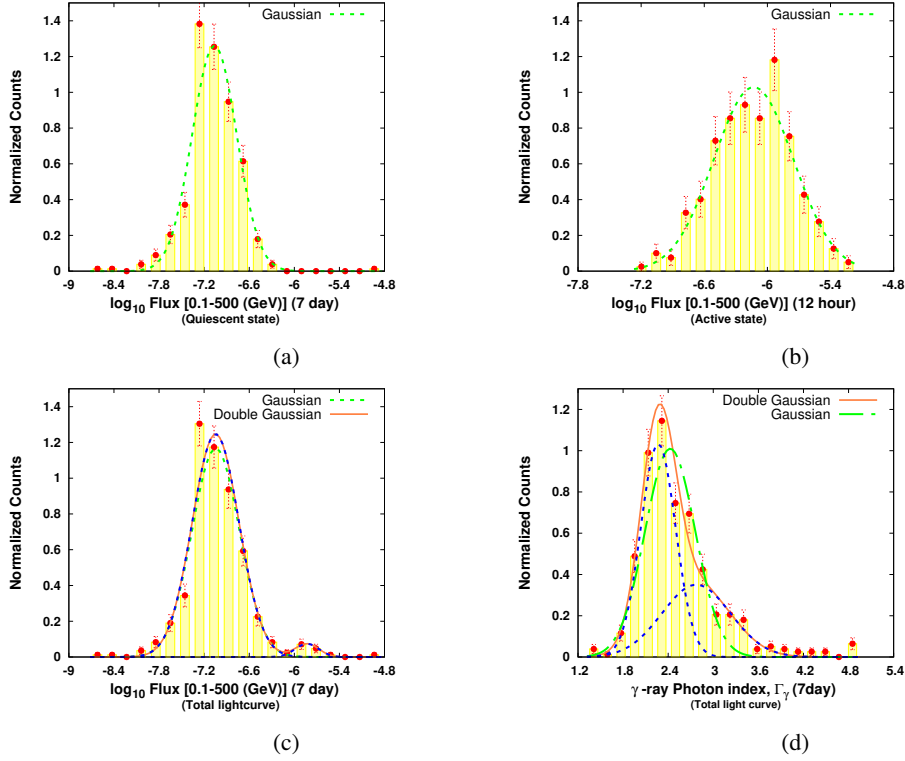


**Figure 10:** Plots showing the histogram fitting of logarithm flux distributions obtained for a) Quiescent state, b) Active state, c) Total lightcurve, and d) The index distribution obtained from the total 7 day binned lightcurve.

**Table 7**

Best fit parameter values of the PDF functions fitted to the logarithm of flux and index histogram. (PDF: GI stands for Gaussian and GII for double Gaussian)

	Histogram	PDF	$\mu_1$	$\sigma_1$	$\mu_2$	$\sigma_2$	$a_1$	$\chi^2/\text{dof}$
7 day binned (Quiescent state)	log10(Flux)	GI	$-7.1 \pm 0.02$	$0.30 \pm 0.01$			$0.93 \pm 0.07$	2.2
	Index	GI	$2.4 \pm 0.03$	$0.3 \pm 0.02$			$0.84 \pm 0.08$	3.9
		GII	$2.3 \pm 0.03$	$0.23 \pm 0.04$	$2.8 \pm 0.2$	$0.45 \pm 0.08$	$0.60 \pm 0.2$	1.8
12 hour binned (Active)	log10(Flux)	GI	$-6.1 \pm 0.01$	$0.40 \pm 0.01$			$1.0 \pm 0.04$	0.7
	Index	GI	$2.1 \pm 0.03$	$0.24 \pm 0.02$			$0.83 \pm 0.1$	4.5
		GII	$2.0 \pm 0.01$	$0.20 \pm 0.01$	$2.5 \pm 0.1$	$0.40 \pm 0.05$	$0.64 \pm 0.09$	0.7
7 day binned (Total)	log10(Flux)	GI	$-7.0 \pm 0.02$	$0.31 \pm 0.02$			$0.92 \pm 0.07$	2.8
		GII	$-7.0 \pm 0.02$	$0.31 \pm 0.01$	$-5.8 \pm 0.07$	$0.16 \pm 0.06$	$1.0 \pm 0.01$	2.2
	Index	GI	$2.4 \pm 0.04$	$0.37 \pm 0.03$			$0.9 \pm 0.09$	3.9
		GII	$2.3 \pm 0.04$	$0.21 \pm 0.04$	$2.6 \pm 0.08$	$0.50 \pm 0.04$	$0.45 \pm 0.1$	1.8

we identified 3 epochs featuring prominent flare. The shortest variability timescale of  $5.5 \pm 0.7$  hours has been found from the variability analysis performed using 12 hour binned lightcurve. The comparison of fluxes in the energy ranges 0.1-1 GeV and 1-500 GeV indicates that this outburst can be majorly caused by the low-energy electrons in the particle distribution. The  $\gamma$ -ray SEDs corresponding to flaring and quiescent states have been studied using various models, revealing that the spectra during the flares exhibit significant curvature/break.

The maximum photon energy, detected positionally consistent with the source, is  $\sim 82$  GeV, and this implies that the emission region may be situated outside the BLR.

Using the pair production opacity argument and considering variability time scale, we obtained the value of minimum jet Doppler factor corresponding to the flaring state as 17 and 13 for the quiescent state. The upper limit on the emission region size has been estimated as  $\sim 10^{16}$  cm.

Further, we performed a detailed statistical broadband SED study of 3 multi-wavelength spectra representing flaring and quiescent activities. Using a one-zone leptonic model that incorporates synchrotron, SSC, and EC emission processes, the observed fluxes at considered energy bands have been successfully reproduced. Interestingly, the observed  $\gamma$ -ray fluxes are well accounted for by attributing

**Table 8**

Results of the Anderson Darling test done for the flux/index distributions. The corresponding distributions will follow a normal only when the statistics becomes lesser than critical value.

	Number of data points	Normal (Flux) AD(critical value)	Normal (log Flux) AD(critical value)	Normal (Spectral index) AD(critical value)
7 day binned Quiescent state	1354	124 (0.779)	2.44 (0.779)	12.8 (0.779)
12 hour binned active state	326	15.2 (0.776)	0.48 (0.776)	10.9 (0.776)
7 day binned total	5850	118 (0.78)	5.9 (0.78)	13.3 (0.78)

them with the external Compton process involving IR photons from the torus. Further the value of observed cooling timescale,  $\tau_c^{\text{obs}}$  estimated from the broadband SED results, closely aligns with the values of time scales obtained from the variability analysis. Our study supports the idea that the  $\gamma$ -ray production in 4C 31.03 happens beyond the BLR, but within the molecular torus.

The study of the variability of the  $\gamma$ -ray emission from 4C 31.03 has been extended by performing a comprehensive long-term distribution study. The  $\gamma$ -ray emission from 4C 31.03 exhibits log-normal variability and showcase a double flux state corresponding to the prolonged quiescent and the recent active phases. The observed log-normal flux distribution can be attributed to the Fermi acceleration processes inside the jet. The index distribution also deviates significantly from normal and features a double normal variability. This may infer that the  $\gamma$ -ray spectrum can be more accurately described by two photon indices rather than a single one.

## Acknowledgements

The authors thank Zahir Shah and Vaidehi S. Paliya for their valuable suggestions. This work has made use of observations from NASA's Fermi gamma-ray and Swift telescopes. The data used in this work were obtained from archives available at Fermi gamma-ray telescope support centre, a service of the Goddard Space Flight Center and the Smithsonian Astrophysical Observatory and NASA's High Energy Astrophysics Science Archive Research Center (HEASARC). AT is thankful to UGC-SAP and FIST 2 (SR/FIST/PS1-159/2010) (DST, Government of India) for the research facilities provided in the Department of Physics, University of Calicut.

## Data Availability

The data used in this paper are publicly available from the archives at <https://heasarc.gsfc.nasa.gov/> and <https://fermi.gsfc.nasa.gov/>.

## References

- [1] S. Ciprini, S. Garrappa, Fermi LAT detection of a GeV gamma-ray flare from blazar 4C +31.03 (B2 0110+31), *The Astronomer's Telegram* 15841 (2023) 1.
- [2] D. Wills, B. J. Wills, Spectroscopy of 206 QSO candidates and radio galaxies., *ApJS* 31 (1976) 143–162. doi:10.1086/190378.
- [3] S. Abdollahi, F. Acero, M. Ackermann, M. Ajello, W. B. Atwood, M. Axelsson, L. Baldini, J. Ballet, G. Barbiellini, D. Bastieri, J. Becerra Gonzalez, R. Bellazzini, A. Berretta, E. Bissaldi, R. D. Blandford, E. D. Bloom, R. Bonino, E. Bottacini, T. J. Brandt, J. Bregeon, P. Bruel, R. Buehler, T. H. Burnett, S. Buson, R. A. Cameron, R. Caputo, P. A. Caraveo, J. M. Casandjian, D. Castro, E. Cavazzuti, E. Charles, S. Chaty, S. Chen, C. C. Cheung, G. Chiaro, S. Ciprini, J. Cohen-Tanugi, L. R. Cominsky, J. Coronado-Blázquez, D. Costantin, A. Cuoco, S. Cutini, F. D'Ammando, M. DeKlotz, P. de la Torre Luque, F. de Palma, A. Desai, S. W. Digel, N. Di Lalla, M. Di Mauro, L. Di Venere, A. Domínguez, D. Dumora, F. Fana Dirirsa, S. J. Fegan, E. C. Ferrara, A. Franckowiak, Y. Fukazawa, S. Funk, P. Fusco, F. Gargano, D. Gasparrini, N. Giglietto, P. Giommi, F. Giordano, M. Giroletti, T. Glanzman, D. Green, I. A. Grenier, S. Griffin, M. H. Grondin, J. E. Grove, S. Guiriec, A. K. Harding, K. Hayashi, E. Hays, J. W. Hewitt, D. Horan, G. Jóhannesson, T. J. Johnson, T. Kamae, M. Kerr, D. Kocevski, M. Kovac'evic', M. Kuss, D. Landriu, S. Larsson, L. Latronico, M. Lemoine-Goumard, J. Li, I. Liodakis, F. Longo, F. Loparco, B. Lott, M. N. Lovellette, P. Lubrano, G. M. Madejski, S. Maldera, D. Malyshev, A. Manfreda, E. J. Marchesini, L. Marcotulli, G. Martí-Devesa, P. Martin, F. Massaro, M. N. Mazziotta, J. E. McEnery, I. Mereu, M. Meyer, P. F. Michelson, N. Mirabal, T. Mizuno, M. E. Monzani, A. Morselli, I. V. Moskalenko, M. Negro, E. Nuss, R. Ojha, N. Omodei, M. Orienti, E. Orlando, J. F. Ormes, M. Palatiello, V. S. Paliya, D. Paneque, Z. Pei, H. Peña-Herazo, J. S. Perkins, M. Persic, M. Pesce-Rollins, V. Petrosian, L. Petrov, F. Piron, H. Poon, T. A. Porter, G. Principe, S. Rainò, R. Rando, M. Razzano, S. Razzaque, A. Reimer, O. Reimer, Q. Remy, T. Reposeur, R. W. Romani, P. M. Saz Parkinson, F. K. Schinzel, D. Serini, C. Sgrò, E. J. Siskind, D. A. Smith, G. Spandre, P. Spinelli, A. W. Strong, D. J. Suson, H. Tajima, M. N. Takahashi, D. Tak, J. B. Thayer, D. J. Thompson, L. Tibaldo, D. F. Torres, E. Torresi, J. Valverde, B. Van Klaveren, P. van Zyl, K. Wood, M. Yassine, G. Zaharijas, Fermi Large Area Telescope Fourth Source Catalog, *ApJS* 247 (2020) 33. doi:10.3847/1538-4365/ab6bcb. arXiv:1902.10045.
- [4] Y.-L. Chang, B. Arsioli, W. Li, D. Xu, L. Chen, Hunting for Neutrino Emission from Multifrequency Variable Sources, *ApJ* 939 (2022) 123. doi:10.3847/1538-4357/ac8c32. arXiv:2203.16740.
- [5] S. Hori, IceCube Collaboration, 4C +31.03: Upper limits from a neutrino search with IceCube, *The Astronomer's Telegram* 15889 (2023) 1.
- [6] S. Cutini, Fermi-LAT detection of enhanced gamma-ray activity from FSRQ 4C +31.03, *The Astronomer's Telegram* 16068 (2023) 1.
- [7] C. M. Urry, P. Padovani, Unified Schemes for Radio-Loud Active Galactic Nuclei, *PASP* 107 (1995) 803. doi:10.1086/133630. arXiv:astro-ph/9506063.
- [8] G. Ghisellini, A. Celotti, L. Costamante, Low power BL Lacertae objects and the blazar sequence. Clues on the particle acceleration process, *A&A* 386 (2002) 833–842. doi:10.1051/0004-6361:20020275. arXiv:astro-ph/0202367.
- [9] G. Ghisellini, A. Celotti, G. Fossati, L. Maraschi, A. Comastri, A theoretical unifying scheme for gamma-ray bright blazars, *MNRAS* 301 (1998) 451–468. doi:10.1046/j.1365-8711.1998.02032.x. arXiv:astro-ph/9807317.
- [10] R. C. Hartman, D. L. Bertsch, S. D. Bloom, A. W. Chen, P. Deines-Jones, J. A. Esposito, C. E. Fichtel, D. P. Friedlander, S. D. Hunter,

- L. M. McDonald, P. Sreekumar, D. J. Thompson, B. B. Jones, Y. C. Lin, P. F. Michelson, P. L. Nolan, W. F. Tompkins, G. Kanbach, H. A. Mayer-Hasselwander, A. Mücke, M. Pohl, O. Reimer, D. A. Kniffen, E. J. Schneid, C. von Montigny, R. Mukherjee, B. L. Dingus, The Third EGRET Catalog of High-Energy Gamma-Ray Sources, *ApJS* 123 (1999) 79–202. doi:10.1086/313231.
- [11] M. S. Shaw, R. W. Romani, G. Cotter, S. E. Healey, P. F. Michelson, A. C. S. Readhead, J. L. Richards, W. Max-Moerbeck, O. G. King, W. J. Potter, Spectroscopy of the Largest Ever  $\gamma$ -Ray-selected BL Lac Sample, *ApJ* 764 (2013) 135. doi:10.1088/0004-637X/764/2/135. arXiv:1301.0323.
- [12] G. Ghisellini, F. Tavecchio, The blazar sequence: a new perspective, *MNRAS* 387 (2008) 1669–1680. doi:10.1111/j.1365-2966.2008.13360.x. arXiv:0802.1918.
- [13] M. Cerruti, Leptonic and Hadronic Radiative Processes in Supermassive-Black-Hole Jets, arXiv e-prints (2020) arXiv:2012.13302. arXiv:2012.13302.
- [14] S. Sahayanathan, S. Godambe, Modelling the very high energy flare of 3C 279 using one-zone leptonic model, *MNRAS* 419 (2012) 1660–1666. doi:10.1111/j.1365-2966.2011.19829.x. arXiv:1109.2442.
- [15] G. B. Rybicki, A. P. Lightman, Radiative Processes in Astrophysics, 1986.
- [16] M. Joshi, A. Marscher, M. Böttcher, Constraining the location of gamma-ray emission in blazar jets. High-energy emission in Blazars, in: *European Physical Journal Web of Conferences*, volume 61 of *European Physical Journal Web of Conferences*, 2013, p. 05004. doi:10.1051/epjconf/20136105004.
- [17] M. Sikora, M. C. Begelman, M. J. Rees, Comptonization of Diffuse Ambient Radiation by a Relativistic Jet: The Source of Gamma Rays from Blazars?, *ApJ* 421 (1994) 153. doi:10.1086/173633.
- [18] C. D. Dermer, R. Schlickeiser, On the Location of the Acceleration and Emission Sites in Gamma-Ray Blazars, *ApJS* 90 (1994) 945. doi:10.1086/191929.
- [19] Z. Shah, S. Sahayanathan, N. Mankuzhiyil, P. Kushwaha, R. Misra, N. Iqbal, Clues on high-energy emission mechanism from blazar 3C 454.3 during 2015 August flare, *MNRAS* 470 (2017) 3283–3299. doi:10.1093/mnras/stx1194. arXiv:1705.06185.
- [20] C. D. Dermer, J. D. Finke, H. Böttcher, Gamma-Ray Studies of Blazars: Synchro-Compton Analysis of Flat Spectrum Radio Quasars, *ApJ* 692 (2009) 32–46. doi:10.1088/0004-637X/692/1/32. arXiv:0808.3185.
- [21] F. A. Aharonian, TeV gamma rays from BL Lac objects due to synchrotron radiation of extremely high energy protons, *New A* 5 (2000) 377–395. doi:10.1016/S1384-1076(00)00039-7. arXiv:astro-ph/0003159.
- [22] M. Cerruti, A. Zech, C. Boisson, S. Inoue, Lepto-hadronic modelling of blazar emission, in: G. Alecian, K. Belkacem, R. Samadi, D. Valls-Gabaud (Eds.), *SF2A-2011: Proceedings of the Annual meeting of the French Society of Astronomy and Astrophysics*, 2011, pp. 555–558. doi:10.48550/arXiv.1111.0557. arXiv:1111.0557.
- [23] M. C. Begelman, B. Rudak, M. Sikora, Consequences of Relativistic Proton Injection in Active Galactic Nuclei, *ApJ* 362 (1990) 38. doi:10.1086/169241.
- [24] A. A. Abdo, M. Ackermann, M. Ajello, E. Antolini, L. Baldini, J. Ballet, G. Barbiellini, D. Bastieri, K. Bechtol, R. a. Bellazzini, Gamma-ray Light Curves and Variability of Bright Fermi-detected Blazars, *ApJ* 722 (2010) 520–542. doi:10.1088/0004-637X/722/1/520. arXiv:1004.0348.
- [25] V. S. Paliya, Fermi-Large Area Telescope Observations of the Exceptional Gamma-Ray Flare from 3C 279 in 2015 June, *ApJ* 808 (2015) L48. doi:10.1088/2041-8205/808/2/L48. arXiv:1507.03073.
- [26] F. Tavecchio, G. Ghisellini, G. Bonnoli, G. Ghirlanda, Constraining the location of the emitting region in Fermi blazars through rapid  $\gamma$ -ray variability, *MNRAS* 405 (2010) L94–L98. doi:10.1111/j.1745-3933.2010.00867.x. arXiv:1003.3475.
- [27] C. D. Dermer, R. Schlickeiser, On the Location of the Acceleration and Emission Sites in Gamma-Ray Blazars, *ApJS* 90 (1994) 945. doi:10.1086/191929.
- [28] R. D. Blandford, A. Levinson, Pair Cascades in Extragalactic Jets. I. Gamma Rays, *ApJ* 441 (1995) 79. doi:10.1086/175338.
- [29] L. Dondi, G. Ghisellini, Gamma-ray-loud blazars and beaming, *MNRAS* 273 (1995) 583–595. doi:10.1093/mnras/273.3.583.
- [30] I. Liodakis, M. Petropoulou, Proton Synchrotron Gamma-Rays and the Energy Crisis in Blazars, *ApJ* 893 (2020) L20. doi:10.3847/2041-8213/ab830a. arXiv:2003.10460.
- [31] P. A. Evans, A. P. Beardmore, K. L. Page, J. P. Osborne, P. T. O’Brien, R. Willingale, R. L. C. Starling, D. N. Burrows, O. Godet, L. Vetere, J. Racusin, M. R. Goad, K. Wiersema, L. Angelini, M. Capalbi, G. Chincarini, N. Gehrels, J. A. Kennea, R. Margutti, D. C. Morris, C. J. Mountford, C. Pagani, M. Perri, P. Romano, N. Tanvir, Methods and results of an automatic analysis of a complete sample of Swift-XRT observations of GRBs, *MNRAS* 397 (2009) 1177–1201. doi:10.1111/j.1365-2966.2009.14913.x. arXiv:0812.3662.
- [32] K. A. Arnaud, XSPEC: The First Ten Years, in: G. H. Jacoby, J. Barnes (Eds.), *Astronomical Data Analysis Software and Systems V*, volume 101 of *Astronomical Society of the Pacific Conference Series*, 1996, p. 17.
- [33] P. M. W. Kalberla, W. B. Burton, D. Hartmann, E. M. Arnal, E. Bajaja, R. Morris, W. G. L. Pöppel, The Leiden/Argentine/Bonn (LAB) Survey of Galactic HI. Final data release of the combined LDS and IAR surveys with improved stray-radiation corrections, *A&A* 440 (2005) 775–782. doi:10.1051/0004-6361:20041864. arXiv:astro-ph/0504140.
- [34] E. F. Schlafly, D. P. Finkbeiner, Measuring Reddening with Sloan Digital Sky Survey Stellar Spectra and Recalibrating SFD, *ApJ* 737 (2011) 103. doi:10.1088/0004-637X/737/2/103. arXiv:1012.4804.
- [35] M. Meyer, J. D. Scargle, R. D. Blandford, Characterizing the Gamma-Ray Variability of the Brightest Flat Spectrum Radio Quasars Observed with the Fermi LAT, *ApJ* 877 (2019) 39. doi:10.3847/1538-4357/ab1651. arXiv:1902.02291.
- [36] S. M. Wagner, P. Burd, D. Dorner, K. Mannheim, S. Buson, A. Gokus, G. Madejski, J. Scargle, A. Arbet-Engels, D. Baack, M. Balbo, A. Bland, T. Bretz, J. Buss, D. Elsaesser, L. Eisenberger, D. Hildebrand, R. Iotov, A. Kalenski, D. Neise, M. Noethe, A. Paravac, W. Rhode, B. Schleicher, V. Sliusar, R. Walter, Statistical properties of flux variations in blazar light curves at GeV and TeV energies, in: *37th International Cosmic Ray Conference*, 2022, p. 868. doi:10.22323/1.395.0868. arXiv:2110.14797.
- [37] D. J. Eisenstein, P. Hut, HOP: A New Group-Finding Algorithm for N-Body Simulations, *ApJ* 498 (1998) 137–142. doi:10.1086/305535. arXiv:astro-ph/9712200.
- [38] L. Foschini, G. Bonnoli, G. Ghisellini, G. Tagliaferri, F. Tavecchio, A. Stamerra, Fermi/LAT detection of extraordinary variability in the gamma-ray emission of the blazar PKS 1510-089, *A&A* 555 (2013) A138. doi:10.1051/0004-6361/201321675. arXiv:1304.2878.
- [39] G. Ghisellini, F. Tavecchio, Canonical high-power blazars, *MNRAS* 397 (2009) 985–1002. doi:10.1111/j.1365-2966.2009.15007.x. arXiv:0902.0793.
- [40] L. Foschini, G. Ghisellini, F. Tavecchio, G. Bonnoli, A. Stamerra, Search for the shortest variability at gamma rays in flat-spectrum radio quasars, *A&A* 530 (2011) A77. doi:10.1051/0004-6361/201117064. arXiv:1101.1085.
- [41] R. A. Edelson, J. H. Krolik, The Discrete Correlation Function: A New Method for Analyzing Unevenly Sampled Variability Data, *ApJ* 333 (1988) 646. doi:10.1086/166773.
- [42] R. Prince, Broadband Variability and Correlation Study of 3C 279 during Flares of 2017&A2018, *ApJ* 890 (2020) 164. doi:10.3847/1538-4357/ab6b1e. arXiv:2001.04493.
- [43] R. Prince, R. Khatoun, C. S. Stalin, Broad-band study of OQ 334 during its flaring state, *MNRAS* 502 (2021) 5245–5258. doi:10.1093/mnras/stab369. arXiv:2102.03516.
- [44] S.-J. Kang, Y.-G. Zheng, Q. Wu, L. Chen, Y. Yin, On the origin of GeV spectral break for Fermi blazars: 3C 454.3, *MNRAS* 502 (2021) 5875–5881. doi:10.1093/mnras/stab489. arXiv:2102.08962.
- [45] E. Lefa, S. R. Kelner, F. A. Aharonian, On the Spectral Shape of Radiation due to Inverse Compton Scattering Close to the Maximum Cutoff, *ApJ* 753 (2012) 176. doi:10.1088/0004-637X/753/2/176.

- arXiv:1205.2929.
- [46] J. Poutanen, B. Stern, GeV Breaks in Blazars as a Result of Gamma-ray Absorption Within the Broad-line Region, *ApJ* 717 (2010) L118–L121. doi:10.1088/2041-8205/717/2/L118. arXiv:1005.3792.
- [47] L. Costamante, S. Cutini, G. Tosti, E. Antolini, A. Tramacere, On the origin of gamma-rays in Fermi blazars: beyond the broad-line region, *MNRAS* 477 (2018) 4749–4767. doi:10.1093/mnras/sty887. arXiv:1804.02408.
- [48] H. T. Liu, J. M. Bai, Absorption of 10-200 GeV Gamma Rays by Radiation from Broad-Line Regions in Blazars, *ApJ* 653 (2006) 1089–1097. doi:10.1086/509097. arXiv:0807.3135.
- [49] S. Sahayanathan, A. Sinha, R. Misra, Broadband spectral fitting of blazars using XSPEC, *Research in Astronomy and Astrophysics* 18 (2018) 035. doi:10.1088/1674-4527/18/3/35. arXiv:1801.00685.
- [50] C. D. Dermer, M. Cerruti, B. Lott, C. Boisson, A. Zech, Equipartition Gamma-Ray Blazars and the Location of the Gamma-Ray Emission Site in 3C 279, *ApJ* 782 (2014) 82. doi:10.1088/0004-637X/782/2/82. arXiv:1304.6680.
- [51] G. R. Burbidge, Estimates of the Total Energy in Particles and Magnetic Field in the Non-Thermal Radio Sources., *ApJ* 129 (1959) 849–852. doi:10.1086/146680.
- [52] S. Saito, Ł. Stawarz, Y. T. Tanaka, T. Takahashi, G. Madejski, F. D’Ammando, Very Rapid High-amplitude Gamma-Ray Variability in Luminous Blazar PKS 1510-089 Studied with Fermi-LAT, *ApJ* 766 (2013) L11. doi:10.1088/2041-8205/766/1/L11. arXiv:1302.0335.
- [53] E. Massaro, A. Tramacere, M. Perri, P. Giommi, G. Tosti, Log-parabolic spectra and particle acceleration in blazars. III. SSC emission in the TeV band from Mkn501, *A&A* 448 (2006) 861–871. doi:10.1051/0004-6361:20053644. arXiv:astro-ph/0511673.
- [54] C. Romoli, N. Chakraborty, D. Dorner, A. Taylor, M. Blank, Flux Distribution of Gamma-Ray Emission in Blazars: The Example of Mrk 501, *Galaxies* 6 (2018) 135. doi:10.3390/galaxies6040135. arXiv:1812.06204.
- [55] S. Vaughan, R. Edelson, R. S. Warwick, P. Uttley, On characterizing the variability properties of X-ray light curves from active galaxies, *MNRAS* 345 (2003) 1271–1284. doi:10.1046/j.1365-2966.2003.07042.x. arXiv:astro-ph/0307420.
- [56] F. M. Rieger, Gamma-Ray Astrophysics in the Time Domain, *Galaxies* 7 (2019) 28. doi:10.3390/galaxies7010028. arXiv:1901.10216.
- [57] P. Uttley, I. M. McHardy, S. Vaughan, Non-linear X-ray variability in X-ray binaries and active galaxies, *MNRAS* 359 (2005) 345–362. doi:10.1111/j.1365-2966.2005.08886.x. arXiv:astro-ph/0502112.
- [58] R. Narayan, T. Piran, Variability in blazars: clues from PKS 2155-304, *MNRAS* 420 (2012) 604–612. doi:10.1111/j.1365-2966.2011.20069.x. arXiv:1107.5812.
- [59] M. Ackermann, R. Anantua, K. Asano, L. Baldini, G. Barbiellini, D. Bastieri, J. Becerra Gonzalez, R. Bellazzini, E. Bissaldi, R. D. Blandford, E. D. Bloom, R. A. Bonino, E. Bottacini, P. Bruel, R. Buehler, G. A. Caliandro, R. A. Cameron, M. Caragiulo, P. A. Caraveo, E. Cavazzuti, C. Cecchi, C. C. Cheung, J. Chiang, G. Chiaro, S. Ciprini, J. Cohen-Tanugi, F. Costanza, S. Cutini, F. D’Ammando, F. de Palma, R. Desiante, S. W. Digel, N. Di Lalla, M. Di Mauro, L. Di Venere, P. S. Drell, C. Favuzzi, S. J. Fegan, E. C. Ferrara, Y. Fukazawa, S. Funk, P. Fusco, F. Gargano, D. Gasparrini, N. Giglietto, F. Giordano, M. Giroletti, I. A. Grenier, L. Guillemot, S. Guiriec, M. Hayashida, E. Hays, D. Horan, G. Jóhannesson, S. Kensei, D. Koccevski, M. Kuss, G. La Mura, S. Larsson, L. Latronico, J. Li, F. Longo, F. Loparco, B. Lott, M. N. Lovellette, P. Lubrano, G. M. Madejski, J. D. Magill, S. Maldera, A. Manfreda, M. Mayer, M. N. Mazziotta, P. F. Michelson, N. Mirabal, T. Mizuno, M. E. Monzani, A. Morselli, I. V. Moskalenko, K. Nalewajko, M. Negro, E. Nuss, T. Ohsugi, E. Orlando, D. Paneque, J. S. Perkins, M. Pesce-Rollins, F. Piron, G. Pivato, T. A. Porter, G. Principe, R. Rando, M. Razzano, S. Razaque, A. Reimer, J. D. Scargle, C. Sgrò, M. Sikora, D. Simone, E. J. Siskind, F. Spada, P. Spinelli, Ł. Stawarz, J. B. Thayer, D. J. Thompson, D. F. Torres, E. Troja, Y. Uchiyama, Y. Yuan, S. Zimmer, Minute-timescale >100 MeV  $\gamma$ -ray Variability during the Giant Outburst of Quasar 3C 279 Observed by Fermi-LAT in 2015 June, *ApJ* 824 (2016) L20. doi:10.3847/2041-8205/824/2/L20. arXiv:1605.05324.
- [60] A. Shukla, K. Mannheim, S. R. Patel, J. Roy, V. R. Chitnis, D. Dorner, A. R. Rao, G. C. Anupama, C. Wendel, Short-timescale  $\gamma$ -Ray Variability in CTA 102, *ApJ* 854 (2018) L26. doi:10.3847/2041-8213/aaacca.
- [61] A. Sinha, R. Khatoun, R. Misra, S. Sahayanathan, S. Mandal, R. Gogoi, N. Bhatt, The flux distribution of individual blazars as a key to understand the dynamics of particle acceleration, *MNRAS* 480 (2018) L116–L120. doi:10.1093/mnras/1807/sly136. arXiv:1807.09073.
- [62] R. Khatoun, Z. Shah, R. Misra, R. Gogoi, Study of long-term flux and photon index distributions of blazars using RXTE observations, *MNRAS* 491 (2020) 1934–1940. doi:10.1093/mnras/stz3108. arXiv:1910.14352.
- [63] G. Bhatta, N. Dhital, The Nature of  $\gamma$ -Ray Variability in Blazars, *ApJ* 891 (2020) 120. doi:10.3847/1538-4357/ab7455. arXiv:1911.08198.
- [64] Z. Shah, N. Mankuzhiyil, A. Sinha, R. Misra, S. Sahayanathan, N. Iqbal, Log-normal flux distribution of bright Fermi blazars, *Research in Astronomy and Astrophysics* 18 (2018) 141. doi:10.1088/1674-4527/18/11/141. arXiv:1805.04675.
- [65] A. Thekkoth, S. Sahayanathan, Z. Shah, V. S. Paliya, C. D. Ravikumar, Understanding the broad-band emission process of 3C 279 through long term spectral analysis, *MNRAS* 526 (2023) 6364–6380. doi:10.1093/mnras/stad3094. arXiv:2310.06819.
- [66] J. Xu, S. Hu, J. R. Webb, G. Bhatta, Y. Jiang, X. Chen, S. Alexeeva, Y. Li, Statistical Analysis of Microvariability Properties of the Blazar S5 0716+714, *ApJ* 884 (2019) 92. doi:10.3847/1538-4357/ab3e50. arXiv:1909.03129.
- [67] H. E. S. S. Collaboration, H. Abdalla, A. Abramowski, F. Aharonian, F. Ait Benkhali, A. G. Akhperjanian, T. Andersson, E. O. Angüner, M. Arrieta, P. Aubert, M. Backes, A. Balzer, M. Barnard, Y. Becherini, J. Becker Tjus, D. Berge, S. Bernhard, K. Bernlöhr, R. Blackwell, M. Böttcher, C. Boisson, J. Bolmont, P. Bordas, J. Bregeon, F. Brun, P. Brun, M. Bryan, T. Bulik, M. Capasso, J. Carr, S. Casanova, M. Cerruti, N. Chakraborty, R. Chalme-Calvet, R. C. G. Chaves, A. Chen, J. Chevalier, M. Chréien, S. Colafrancesco, G. Cologna, B. Condon, J. Conrad, Y. Cui, I. D. Davids, J. Decock, B. Degrange, C. Deil, J. Devin, P. deWilt, L. Dirson, A. Djannati-Ataï, V. Domainko, A. Donath, L. O. C. Drury, G. Dubus, K. Dutton, J. Dyks, T. Edwards, K. Egberts, P. Eger, J. P. Ernenwein, S. Eschbach, C. Farnier, S. Fegan, M. V. Fernandes, A. Fiasson, G. Fontaine, A. Förster, S. Funk, M. Füßling, S. Gabici, M. Gajdus, Y. A. Gallant, T. Garrigoux, G. Giavitto, B. Giebels, J. F. Glicenstein, D. Gottschall, A. Goyal, M. H. Grondin, D. Hadasch, J. Hahn, M. Haupt, J. Hawkes, G. Heinzelmann, G. Henri, G. Hermann, O. Hervet, J. A. Hinton, W. Hofmann, C. Hoischen, M. Holler, D. Horns, A. Ivascenko, A. Jacholkowska, M. Jamroz, M. Janiak, D. Jankowsky, F. Jankowsky, M. Jingo, T. Jogler, L. Jouvin, I. Jung-Richardt, M. A. Kastendieck, K. Katarzyński, U. Katz, D. Kerszberg, B. Khélifi, M. Kieffer, J. King, S. Klepser, D. Klochov, W. Kluzniak, D. Kolitzus, N. Komin, K. Kosack, S. Krakau, M. Kraus, F. Krayzel, P. P. Krüger, H. Laffon, G. Lamanna, J. Lau, J. P. Lees, J. Lefaucheur, V. Lefranc, A. Lemièrre, M. Lemoine-Goumard, J. P. Lenain, E. Leser, T. Lohse, M. Lorentz, R. Liu, R. López-Coto, I. Lypova, V. Marandon, A. Marcowith, C. Mariaud, R. Marx, G. Maurin, N. Maxted, M. Mayer, P. J. Meintjes, M. Meyer, A. M. W. Mitchell, R. Moderski, M. Mohamed, L. Mohrmann, K. Morà, E. Moulin, T. Murach, M. de Naurois, F. Niederwanger, J. Niemiec, L. Oakes, P. O’Brien, H. Odaka, S. Öttl, S. Ohm, M. Ostrowski, I. Oya, M. Padovani, M. Panter, R. D. Parsons, N. W. Pekeur, G. Pelletier, C. Perennes, P. O. Petrucci, B. Peyaud, Q. Piel, S. Pita, H. Poon, D. Prokhorov, H. Prokoph, G. Pühlhofer, M. Punch, A. Quirrenbach, S. Raab, A. Reimer, O. Reimer, M. Renaud, R. de los Reyes, F. Rieger, C. Romoli, S. Rosier-Lees, G. Rowell, B. Rudak, C. B. Rulten, V. Sahakian, D. Salek, D. A. Sanchez, A. Santangelo, M. Sasaki, R. Schlickeiser, F. Schüssler, A. Schulz, U. Schwanke, S. Schwemmer, M. Settimo, A. S. Seyffert, N. Shafi, I. Shilon, R. Simoni, H. Sol, F. Spanier, G. Spengler, F. Spies, Ł. Stawarz, R. Steenkamp,

- C. Stegmann, F. Stinzing, K. Stycz, I. Sushch, J. P. Tavernet, T. Tavernier, A. M. Taylor, R. Terrier, L. Tibaldo, D. Tiziani, M. Tluczykont, C. Trichard, R. Tuffs, Y. Uchiyama, D. J. van der Walt, C. van Eldik, C. van Rensburg, B. van Soelen, G. Vasileiadis, J. Veh, C. Venter, A. Viana, P. Vincent, J. Vink, F. Voisin, H. J. Völk, T. Vuillaume, Z. Wadiasingh, S. J. Wagner, P. Wagner, R. M. Wagner, R. White, A. Wierzcholska, P. Willmann, A. Wörnlein, D. Wouters, R. Yang, V. Zabalza, D. Zaborov, M. Zacharias, A. A. Zdziarski, A. Zech, F. Zefi, A. Ziegler, N. Żywucka, Characterizing the  $\gamma$ -ray long-term variability of PKS 2155-304 with H.E.S.S. and Fermi-LAT, *A&A* 598 (2017) A39. doi:10.1051/0004-6361/201629419. arXiv:1610.03311.
- [68] A. Dmytriiev, H. Sol, A. Zech, Connecting steady emission and very high energy flaring states in blazars: the case of Mrk 421, *MNRAS* 505 (2021) 2712–2730. doi:10.1093/mnras/stab1445. arXiv:2105.12480.
- [69] T. R. Lewis, J. D. Finke, P. A. Becker, Electron Acceleration in Blazars: Application to the 3C 279 Flare on 2013 December 20, *ApJ* 884 (2019) 116. doi:10.3847/1538-4357/ab43c3. arXiv:1909.04431.